Geochemistry, Geophysics, Geosystems®

RESEARCH ARTICLE
10.1029/2023GC011425

# Quantitative Insights on Impurities in Ice Cores at the Micro-Scale From Calibrated LA-ICP-MS Imaging

**Pascal Bohleber[1], Piers Larkman[1], Nicolas Stoll[1], David Clases[2], Raquel Gonzalez de Vega[2], Martin Šala[3], Marco Roman[1], and Carlo Barbante[1,4]**

[1]Department of Environmental Sciences, Informatics and Statistics, Ca' Foscari University of Venice, Mestre, Italy, [2]Nano Micro LAB, Institute of Chemistry, University of Graz, Graz, Austria, [3]Department of Analytical Chemistry, National Institute of Chemistry, Ljubljana, Slovenia, [4]Institute of Polar Sciences, CNR, Venice, Italy

**Key Points:**

- This study presents new quantification strategies for two-dimensional micro-scale impurity imaging on ice cores with laser-ablation-inductively-coupled-plasma-mass-spectrometry (LA-ICP-MS)
- Calibrated LA-ICP-MS maps reveal similar spatial distributions of impurities in all ice core samples, while concentrations vary distinctly
- We developed a method to investigate the displacement of impurities by grain growth and to study ice-impurity interactions in the laboratory

**Supporting Information:**

Supporting Information may be found in the online version of this article.

**Correspondence to:**

P. Bohleber,
pascal.bohleber@unive.it

**Citation:**

Bohleber, P., Larkman, P., Stoll, N., Clases, D., Gonzalez de Vega, R., Šala, M., et al. (2024). Quantitative insights on impurities in ice cores at the micro-scale from calibrated LA-ICP-MS imaging. *Geochemistry, Geophysics, Geosystems*, *25*, e2023GC011425. https://doi.org/10.1029/2023GC011425

Received 22 DEC 2023
Accepted 27 FEB 2024

**Abstract** Understanding the microscopic variability of impurities in glacier ice on a quantitative level has importance for assessing the preservation of paleoclimatic signals and enables the study of macroscopic deformational as well as dielectric ice properties. Two-dimensional imaging via laser-ablation-inductively-coupled-plasma-mass-spectrometry (LA-ICP-MS) can provide key insight into the localization of impurities in the ice. So far, these findings are mostly qualitative and gaining quantitative insights remains challenging. Recent advances in LA-ICP-MS high-resolution imaging now allow ice grains and grain boundaries to be resolved individually. These resolutions require new adequate quantification strategies and, consequently, accurate calibration with matrix-matched standards. Here, we present three different quantification methods, which provide a high level of homogeneity at the scale of a few tens of microns and are dedicated to imaging applications of ice cores. One of the proposed methods has a second application, offering laboratory experiments to investigate the displacement of impurities by grain growth, with important future potential to study ice-impurity interactions. Standards were analyzed to enable absolute quantification of impurities in selected ice core samples. Calibrated LA-ICP-MS maps indicate similar spatial distributions of impurities in all samples, while impurity levels vary distinctly: Higher concentrations were detected in glacial periods and Greenland, and lower levels in interglacial periods and samples from central Antarctica. These results are consistent with ranges from complementary meltwater analysis. Further comparison with cm-scale melting techniques calls for a more sophisticated understanding of the ice chemistry across spatial scales, to which calibrated LA-ICP-MS maps now contribute quantitatively.

**Plain Language Summary** Compared to the large amount of information relating to paleoclimate signals reconstructed from cm-scale impurity measurements on ice cores, knowledge about the spatial variability of impurities at the micro-scale is extremely sparse—and becomes even more rare once quantitative datasets are concerned. However, there is an increasing demand for quantitative data for assessing the preservation of paleoclimatic signals and for the study of macroscopic deformational as well as dielectric ice properties in ice flow modeling and remote sensing. Two-dimensional imaging via laser-ablation-inductively-coupled-plasma-mass-spectrometry (LA-ICP-MS) has shown great potential in this context, but so far, gaining reliable quantitative results for micro-scale imaging has not been possible. Here, we present new quantification strategies that finally allow accurate calibration using ice standards. We carefully discuss the pros and cons of each method, apply the calibration to different samples from Greenland and Antarctica, and deliver the first calibrated LA-ICP-MS impurity maps at 40 μm resolution. Our results are consistent with bulk measurements performed on melted samples. The calibrated LA-ICP-MS maps will be essential for further comparison with bulk meltwater analysis, which may ultimately deliver an improved understanding of paleoclimate signals stored in deep ice.



## 1. Introduction

Aerosol-related atmospheric impurity records make up an important part of the unique variety of climate proxies archived in polar ice cores (e.g., Fischer et al., 2021; Legrand & Mayewski, 1997). Depending on the amount of annual net accumulation and layer thinning at the site a core is collected from, meltwater analysis at cm-scale depth resolution, for example, using continuous flow analysis (CFA), can extract information about the vertical impurity variability in ice all the way from millennial to sub-annual time scales (Kaufmann et al., 2008; McConnell et al., 2002; Röthlisberger et al., 2000). Understanding the variability of impurities in the deepest and

most highly thinned ice core layers remains a pressing challenge in ice core research, as new efforts are underway to retrieve climatic records older than 1 million years from Antarctica (Brook et al., 2006; Fischer et al., 2013). Mastering this challenge goes far beyond the current state-of-the-art of analytical techniques and specifically, sub-mm depth resolution is required. This requisition becomes apparent when considering for example, 1 m of an "oldest" ice core section at the "Little Dome C" drill site, which may contain more than 10,000 years (Lilien et al., 2021). A second set of problems arises from post-depositional signal alterations, which have challenged and ultimately hampered the full exploitation of impurity-related climate signals in deep parts of ice cores (e.g., Lambert et al., 2008; Traversi et al., 2009).

In general, ice crystals (from now-on referred to as grains) grow in size over time, especially in deep ice conditions featuring warmer temperatures close to the melting point. Although the underlying mechanisms are still debated, growing grains can displace impurities, which are subsequently preferentially located at the grain boundaries, and can experience drag in their growth due to interactions with inclusions of insoluble impurities (Stoll, Eichler, Hörhold, Shigeyama, & Weikusat, 2021 and references within). The resulting impurity localization—that is, the element-specific three-dimensional distribution of impurities in the ice crystal matrix—has important consequences for further post-depositional processes. Soluble species are especially affected by the diffusion along the network of ice veins and potentially also grain boundaries (Ng, 2021; Rempel et al., 2001). Further post-depositional alterations have also been documented for insoluble impurities, including systematic changes in their size distribution by forming aggregates (Lambert et al., 2008) and englacial chemical reactions between dust particles and acidic environments formed within grain boundaries (Baccolo et al., 2021). In view of these recognized but not fully understood processes, it becomes paramount to understand the spatial impurity variability in deep ice in new detail in order to avoid misunderstanding of high-resolution signals.

To investigate the intricate interplay of impurities with the ice matrix, techniques analyzing ice cores in their solid state have been shown to be indispensable, as important information on the impurity localization in ice is inevitably lost when melting for analysis (Stoll, Bohleber, et al., 2023). Laser ablation inductively coupled plasma mass spectrometry (LA-ICP-MS) offers micron-resolution and micro-destructiveness for ice core impurity analysis (Müller et al., 2011; Sneed et al., 2015). Early on in the use of LA-ICP-MS for ice core analysis, it was recognized that the technique can also reveal the localization of impurities within the ice (Della Lunga et al., 2014, 2017). Recent adaption for two-dimensional high-resolution impurity imaging of ice cores has fully capitalized on this application, with hundreds of adjacent lines measured in parallel over a surface area at a resolution of tens of microns. This delivered unprecedented detail about the impurity localization within the ice matrix (Bohleber et al., 2020). For mostly water-soluble species such as Na, the chemical maps have revealed a high degree of localization at grain boundaries and mostly signal-free grain interiors (Bohleber et al., 2021). Conversely, using 2D LA-ICP-MS imaging of dust-rich samples, such as "cloudy bands," showed localized particle clusters dispersed within the grains, especially for crustal elements such as Al, Si, and Fe (Bohleber et al., 2023; Stoll, Westhoff, et al., 2023).

Comparing LA-ICP-MS signals with cm-scale CFA revealed that the LA-ICP-MS low frequency variability shows qualitatively similar variability to the full resolution meltwater analysis (Della Lunga et al., 2017; Spaulding et al., 2017). However, for deep ice conditions in Antarctica featuring large grains (centimeters to decimeters in diameter), low bulk concentrations, and an expected high degree of impurity localization, it remains unclear how to integrate information about impurities mapped at the grain scale with bulk meltwater analysis. This task is a scale challenge but also has a quantitative dimension: As grain boundaries make up only a small portion of the volume, concentrations of impurities mostly (or entirely) localized in grain boundaries could become high compared to the typical ppb–ppt levels of ionic impurities and trace elements measured in bulk samples (e.g., Legrand & Mayewski, 1997). In this context, quantifying the impurity concentrations at grain boundaries as well as background levels in the grain interior becomes important. Achieving a reliable calibration for LA-ICP-MS, at the scale of imaging, is the key to deliver this information.

Matrix-matched calibrations use standards with known impurity concentrations that also have the same ablation behavior as the sample, which is a known challenge for LA-ICP-MS. Seminal work on using artificial ice samples for calibration has been conducted since the pioneering phase of LA-ICP-MS ice core analysis (Reinhardt et al., 2001; Wilhelms-Dick, 2008) and was later refined to achieve calibrated line profiles and interpolated maps (Della Lunga et al., 2017). The method employed in these studies revolves around sequentially freezing several mL of standard solution to obtain a bulk ice sample. The achieved homogeneity was considered sufficient at the

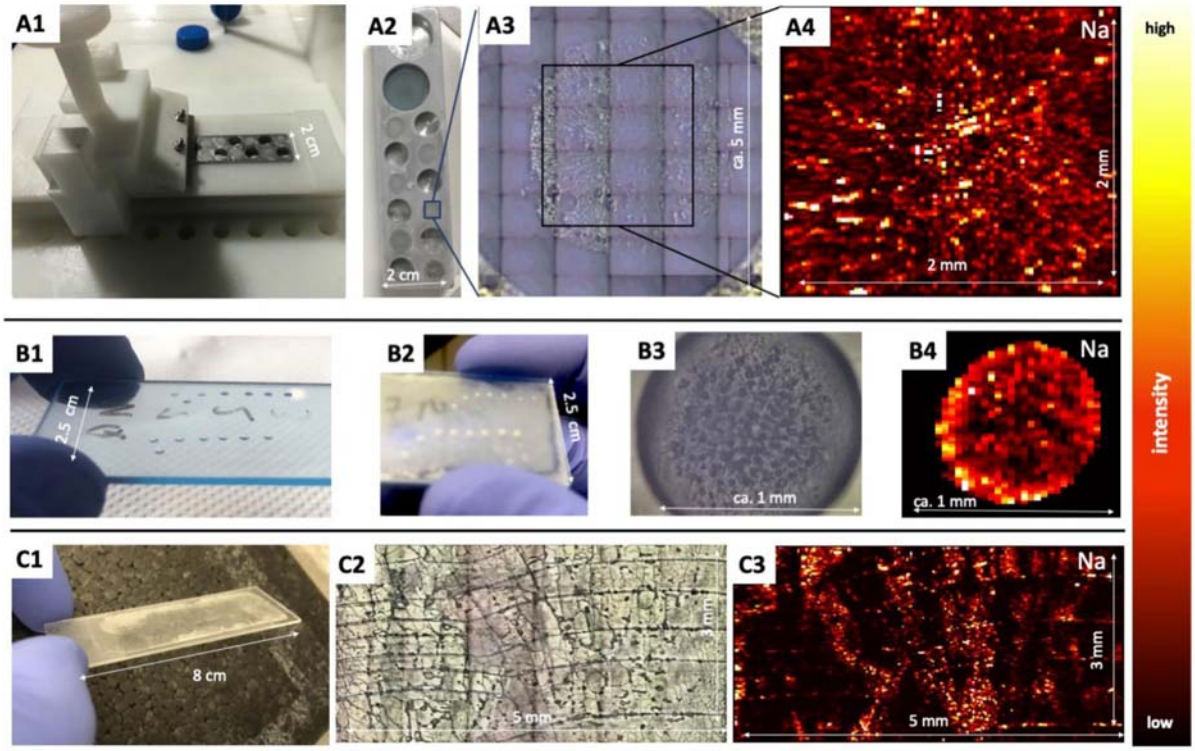


**Figure 1.** Overview on different methods for artificial ice standard preparation with a holder (a), drops on a composite slide (b) and molds (c). Shown for each method from left to right: Photos of the samples (A1, A2, B1, B2, C1), optical mosaics of the ice surface taken with the laser camera (A3, B3, C2) and exemplary laser-ablation-inductively-coupled-plasma-mass-spectrometry maps for Na for a 1,000 ppb standard solution (A4, B4, C3). Also shown is the color scale used throughout the manuscript.

respective resolution level using 200–300 µm spot sizes and slow sample transfer lines. The small spots (20–40 µm) and fast sample transfer used in current state-of-the-art imaging enable an increase in spatial resolution by at least one order of magnitude compared to the earlier studies. This also entails a demand for sufficient homogeneity in ice standards at that scale. As a result, thus far, it remains unclear how a full matrix-matched calibration can be achieved for state-of-the-art ice core imaging.

Here, we report on new approaches to manufacture and utilize artificial ice standards suitable for calibrating LA-ICP-MS imaging. Three methods have been developed for reducing the frozen volume and increasing the speed of the freezing process. By their application at 40 µm resolution, we show how we can obtain quantitative insights on the impurity distribution in ice cores using LA-ICP-MS and provide experimental insight into impurity relocation by grain growth.

## 2. Materials and Methods

### 2.1. Preparation of Artificial Ice Standards by Three Different Methods

Liquid standards were prepared by diluting multi-elemental stock solutions (e.g., Merck IV ICP-MS standard) with Milli-Q water (18.2 MΩ cm, Merck Millipore, Bedford, USA) to a range of concentrations optimized differently for each experiment. Typical concentrations were 50, 100, 200, 400, 800, 1,200, 2,000, and 5,000 ppb (ng $g^{-1}$). Solutions were made freshly for each round of experiments. Blanks from MilliQ water were also included. To achieve a homogeneous distribution of impurities in the ice made from solutions, we attempted to keep the volume of liquid as small as possible to minimize the freezing time. With this strategy, three different methods were developed for making artificial ice, referred to as A, B, and C in the following text (Figure 1).

Method A uses a custom-made sample aluminum holder with six cylindrical holes that are 6 mm in diameter and 3 mm in depth (Figure 1a). Solutions are pipetted into the holes at room temperature, and the sample holder is

subsequently immersed in liquid nitrogen for freezing. To decontaminate the generated ice and achieve a plane surface, the samples are then scraped in a custom-built scraping device housing a ceramic $ZrO_2$ blade (American Cutting Edge, USA) (Bohleber et al., 2020). Adjacent to each standard, an additional larger hole collects the scraped-off material to avoid cross-contamination. The sample holder also features two holes for NIST glass standards.

Method B significantly reduces sample volumes by pipetting a series of 0.5 µL standard solution drops onto a pre-cleaned polycarbonate slide (Figure 1b). The slide is then immediately inserted into a clean polypropylene container, protecting it from further contact with the lab atmosphere, and placed in a freezer at −80°C, guaranteeing almost immediate freezing. The generated ice drops are about (1.1 ± 0.1) mm in diameter. Freezing by pipetting onto the pre-cooled slide in liquid $N_2$ was not possible, which led to freezing before contact with the slide, preventing the drops from attaching to the slide. As an alternative, it is possible to place slides prepared with liquid drops onto a metal block cooled by liquid nitrogen.

Method C uses adhesive chamber molds (Grace Bio-Labs, Figure 1c), which are conventionally used for maintaining bacterial cultures. These molds have previously been suggested for use in manufacturing gelatine-based standards for quantifying elemental distributions in biological samples (Westerhausen et al., 2019). The molds were attached to a pre-cleaned polycarbonate slide and subsequently filled with standard solutions using a pipette. As with method B, these slides were inserted into a clean polypropylene container for further protection. Freezing these slides in liquid $N_2$ damages the molds and causes leaking or spraying of solution during freezing. Hence, freezing again took place in a −80°C freezer. Molds of different volumes were used, for example, a single chamber per slide (65 × 22 × 0.25 mm) or multiple chambers per slide filled with different standards (9.8 × 20 × 0.25 mm).

### 2.2. Imaging of Ice Samples and Standards With LA-ICP-MS

The LA-ICP-MS set-up established for ice core imaging at Ca' Foscari University of Venice comprises an Analyte Excite ArF excimer 193 nm laser (Teledyne CETAC Photon Machines) and an iCAP-RQ quadrupole ICP-MS (Thermo Scientific) connected via an ARIS rapid aerosol transfer line for fast washout. The samples were placed on a custom cryogenic sample holder, where a circulating glycol-water mixture (−35°C) was used to keep the temperature at the sample surface below −(23 ± 2)°C. Ice standards were prepared using one of the methods A, B, or C and inserted into the ablation chamber either independently or alongside ice core samples. Immediately before insertion into the ablation chamber, ice core sample surfaces were freshly decontaminated by scraping with ceramic $ZrO_2$ blades. The imaged areas were further cleaned by preablation with an 80 × 80 µm square laser spot. If not noted otherwise, the reported analysis was carried out using an 40 µm circular laser spot. Washout times for this spot size were determined to be approximately 50 ms, allowing the distribution of dwell times evenly at 10 ms each for $^{23}Na$, $^{24}Mg$, $^{27}Al$, $^{57}Fe$, and $^{88}Sr$. For some experiments, the mass-to-charge ratio of $m/z = 17$ (typically relating to $OH^+$) was also monitored at 10 ms dwell time. The repetition rate and dosage were complementally adjusted to avoid anti-aliasing, for example, 220 Hz at dosage 11 (van Elteren et al., 2020). Unless otherwise stated, the laser fluence was set to 3.5 J $cm^{-2}$. Lines on a NIST612 glass standard were ablated before and after the image acquisition for drift correction. Drift correction and map generation were conducted with the software HDIP (Teledyne Photon Machines). Further details on the ice core imaging procedure are described in Bohleber et al. (2020).

### 2.3. Evaluation of Ice Standards and Ice Core Samples

For method A using the sample holder, a subset of concentration levels had to be chosen for the six holes. Square map sizes up to 2 × 2 mm were typically possible. Method A generally allowed for preablation, with some exceptions for higher concentration ranges (see Section 3.1 below). In Method B, the drops were imaged by setting a square area encompassing the ice and carefully adjusting the laser focus height to the mid-elevation of the drop (Figure 1b). In HDIP or MATLAB, the quasi-circular area of the drops was segmented out from the map for subsequent calculation of the mean and standard deviation. Due to the small volume of the drops, preablation was not feasible without destroying the standards. Due to the large planar surface created by Method C, the molds offered large areas over which maps of several $mm^2$ were taken. Preablation was possible, but fluence had to be reduced to avoid destructive ablation when using large spots.

**Table 1**
*Overview of Ice Core Samples Analyzed With LA-ICP-MS (LA) and in Liquid Bulk Analysis With SP-ICP-TOFMS (LQ)*

| Location | Core name | Bag n° | Size (mm) | Depth (m) | Age (ka BP) | Analysis |
|---|---|---|---|---|---|---|
| East Greenland | EGRIP | 253 | 13 × 17 × 10 | 138.6 | 1[a] | LA |
| | EGRIP | 3316 | 14 × 20 × 10 | 1,823.5 | 34.7[b] | LA |
| | EGRIP | 3424 | 16 × 18 × 10 | 1,883.1 | 37.3[b] | LQ |
| Central Antarctica | EDC | 513 | 79 × 20 × 10 | 281.8 | 9[c] | LQ |
| | EDC | 514 | 79 × 20 × 10 | 282.3 | 9[c] | LA |
| | EDC | 1994 | 79 × 20 × 10 | 1,096.5 | 74[c] | LA & LQ |
| | EDC | 1995 | 79 × 20 × 10 | 1,096.9 | 74[c] | LQ |

[a]Mojtabavi et al. (2020). [b]Gerber et al. (2021). [c]Parrenin et al. (2007).

To evaluate the degree of homogeneity achieved by the different methods, we calculated the relative standard deviation (RSD) as in previous studies using line profiles (Della Lunga et al., 2017; Reinhardt et al., 2001). Based on 2D imaging, however, we were able to consider the variability in intensity by the RSD, and the spatial homogeneity of the impurity distribution in the artificial ice. For this purpose, we used the Distributional Homogeneity Index (DHI) developed by Sacré et al. (2014). The DHI shows a linear relationship with increasing DHI values for decreasing homogeneity, as demonstrated with simulated maps of known homogeneity (Sacré et al., 2014). Uncertainty estimates for the DHI are obtained from multiple runs ($n = 50$) in randomizing the input image, following Sacré et al. (2014).

In order to quantitatively compare a set of ice core samples covering a broad range of ice conditions and impurity concentrations, we measured samples from both Greenland (East Greenland Ice-core Project, EGRIP) and central Antarctica (EPICA Dome C, EDC) as well as glacial and interglacial periods. Table 1 provides an overview. The EGRIP samples were previously analyzed by Cryo-Raman Spectroscopy, bags 253, 3316, and 3424 correspond to sample 1 in Stoll, Eichler, Hörhold, Erhardt, et al. (2021) and samples 7 and 8 in Stoll, Westhoff, et al. (2023), respectively. Samples were measured in pairs of Holocene and glacial samples, with two images collected immediately after another. Analog to a previously employed approach (Bohleber et al., 2023), the maps were analyzed to separate intensities at grain boundaries and grain interiors. For this purpose, pixels belonging to grain boundaries were segmented in HDIP using a watershed algorithm and confronted with regions belonging to the grain interior, taking the average over the entire map.

### 2.4. Analysis of Melted Ice Samples

To provide an additional set of reference values for the bulk impurity concentration, additional ice core samples were brought to the University of Graz where they were analyzed as liquids. Due to limited sample availability, samples for liquid analysis were selected in close proximity to the samples measured using LA-ICP-MS, with one direct comparison possible for EDC1994 (Table 1). The samples were decontaminated by washing with MQ water, then inserted in a clean polypropylene container, left to melt, and analyzed directly after melting. Blank values were obtained by freezing MQ water and following an identical preparation procedure to the samples. Using a "time-of-flight" platform (Vitesse ICP-TOF-MS by Nu Instruments, Wrexham, UK) in a "single particle" configuration made it possible to separate the soluble and particulate contributions to the overall bulk concentration. Instrumental settings are included in Supporting Information S1. The single particle analysis (SP-ICP-TOFMS) was chosen to aid the further comparison with LA-ICP-MS imaging. LA-ICP-MS measures the total concentration (soluble and particulate) but the geochemical signature of particles can be isolated to some extent based on chemical images (Bohleber et al., 2023). The results of the liquid analysis are included in Table S1 in Supporting Information S1.

## 3. Results

### 3.1. Assessing the Homogeneity of Artificial Ice Standards

Imaging offers an improved means to assess the spatial variability of the ice standards for each method. Overall, the best degree of homogeneity was achieved using method B. Typical RSD values are around 10% but differ

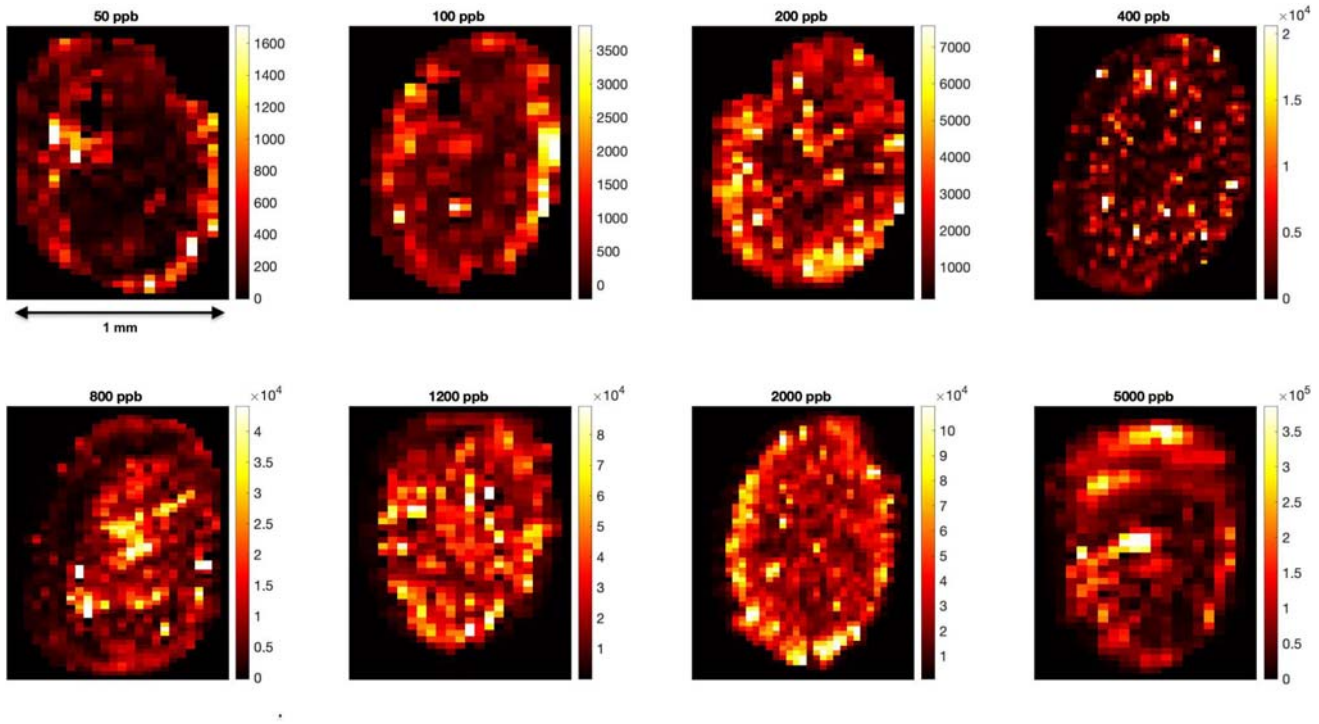


**Figure 2.** Laser-ablation-inductively-coupled-plasma-mass-spectrometry maps for Mg intensities (cts) illustrating a typical degree of homogeneity achieved across a set of drops created using method B over the concentration range used for calibration. Note differences in the values of the intensity color scale.

among the elements in one set of concentrations. Figure 2 shows the example of Mg for the full range in concentrations. Mean RSD values (±1 Standard Error) range between (6 ± 2)% for Al and (13 ± 7)% for Mg. The spatial homogeneity shows mean DHI values around (2.0 ± 0.2), 1.7 for Na up to 2.3 for Al, which corresponds to about 90% homogeneity in synthetic images (Sacré et al., 2014). Method A has similar but slightly higher RSD and DHI values. Within one set (Figure 2), RSD values range from (7 ± 2)% for Al, (12 ± 4)% for Mg to (21 ± 11)% for Sr. Corresponding DHI mean values range from 1.7 for Fe up to 2.5 for Al. All values are summarized in Table S2 in Supporting Information S1.

The homogeneity in the drops was not found to increase when freezing with liquid nitrogen. Since freezing in liquid nitrogen involved a longer exposure of the drops and hence a higher contamination risk, enclosure in polypropylene containers and freezing in the −80°C freezer became our standard method. Contamination was checked against blank ice made from MilliQ water. All methods were found to be sufficiently robust against contamination; typical examples are shown in Supporting Information S1 (Figure S1 in Supporting Information S1). Since method B allows a variable set of concentrations and is faster to prepare and measure, it became the primary choice for calibration experiments.

In spite of the small volume used for preparing the drops, it is generally not possible to completely ablate the entire volume in one run, as compared to studies using droplets of even smaller volume, for example, several 100 pL (Schweikert et al., 2022). An exception is ice made from high-concentration standard solutions, typically more than 10 ppm (μg $g^{-1}$), which appear to ablate more readily than their low-concentration counterparts. This can lead to partial or continuous "uncontrolled" ablation characterized by highly variable ablated volume, manifesting in deep ablation craters with ill-defined edges and substantial noise in output images. Figure 3 provides visual examples of this effect in ice made by method A. In the case of this uncontrolled ablation regime, $m/z = 17$ gives a clear signal above the background. Using $m/z = 17$ to detect this transition and its dependency on lasering conditions, we conducted a series of experiments, varying concentrations (0.002–0.2–2–20–200 ppm), fluence (2–6 J $cm^{-2}$ in 0.5 steps) as well as spot size (20, 40, 65 μm). Figure 3 shows the results. For the 40 μm spot size experiment, it becomes clear that above a fluence of 3.5 J $cm^{-2}$ uncontrolled ablation starts to appear in the region

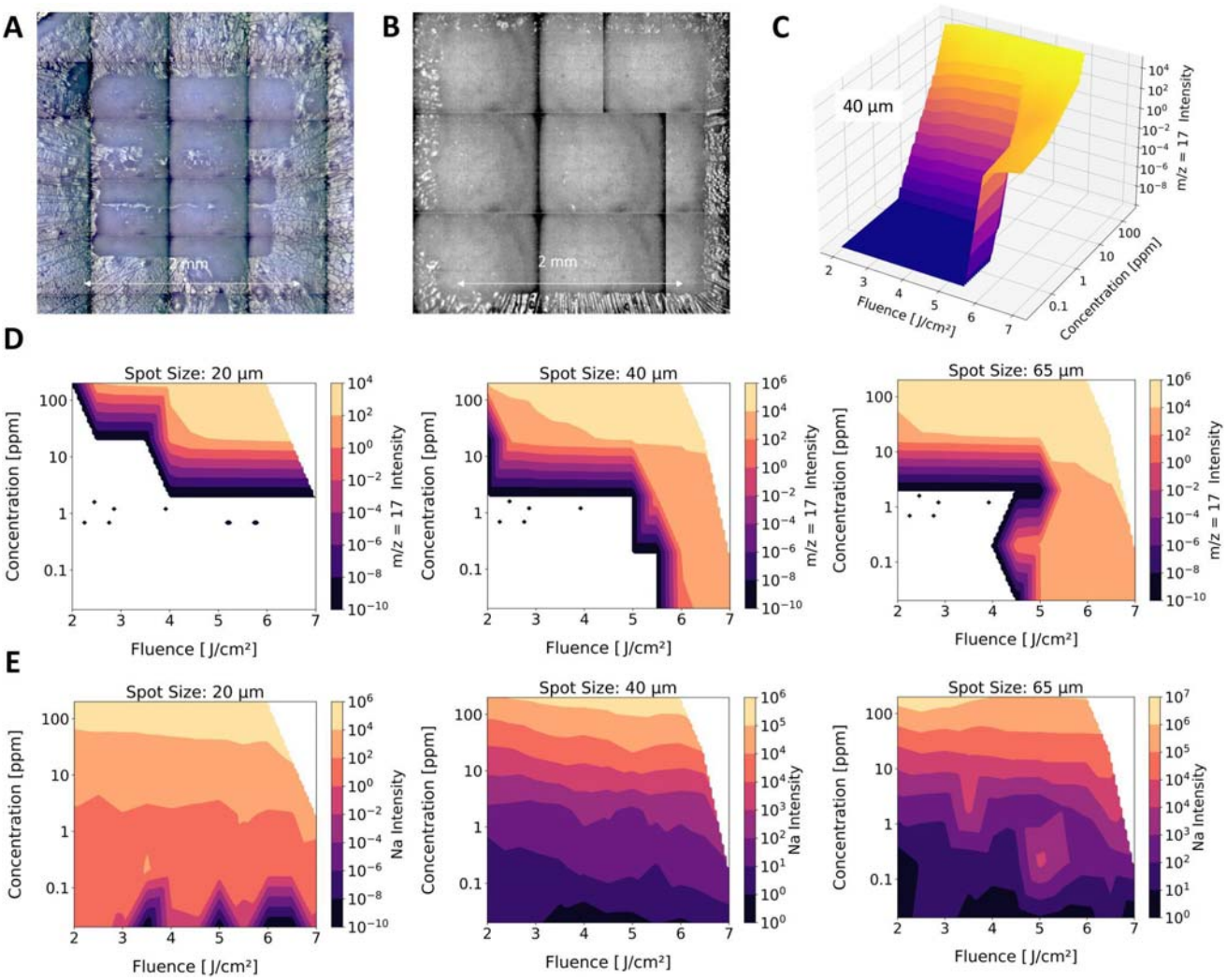


**Figure 3.** Visual examples for partially destructive ablation (a) or continuous destructive ablation (b) on ice standards made from Method A. Panel (c) shows the interpolated signal intensity (log) of $m/z = 17$ as a function of fluence and concentration (log). Panel (d) shows a 2D contour representation for spot sizes of 20, 40, and 65 µm. Uncontrolled ablation dominates within the areas shaded in orange and yellow. Note how the calibration experiments performed here for a 40 µm spot (3.5 J/cm$^2$, concentration levels up to 5 ppm) stay within the controlled ablation regime (panels c and d). Panel (e) shows the corresponding signals for Na. Note the increase in signal intensity especially visible for 65 µm spot size, fluence above 4.5 J cm$^{-2}$ and concentrations below 1 ppm.

above 10 ppm but appears sooner if higher fluences are used. At 65 µm, this transition starts earlier. At 20 µm, ice made from high-concentration solutions can be ablated at comparatively higher fluences.

### 3.2. Impurity Displacement Observed in Artificial Ice

Method C produces a planar-sided slab of ice with a vertical thickness of 250 µm. The mold cover protects the surface from contamination and is removed immediately before the sample is inserted into the ablation chamber. In an optical laser camera, the surfaces typically show microstructural features such as air bubbles and grain boundaries. Due to the freezing process, the surface features small cracks (e.g., horizontal curved dark lines in Figure 1c), which do not significantly affect the impurity distribution and are only visible if the ice is analyzed immediately after freezing. On the scale of the comparatively large images afforded by this method (several square mm), the impurities are often found within patches that initially have no clear association with a specific microstructural feature. If samples are left to age, however, even for just a few days, impurities start to localize at grain boundaries. Figure 4 gives an overview of this effect for Na and Al, as representatives of relatively soluble and insoluble species, respectively. Starting from an initial distribution from ice produced using method C, as

10.1029/2023GC011425

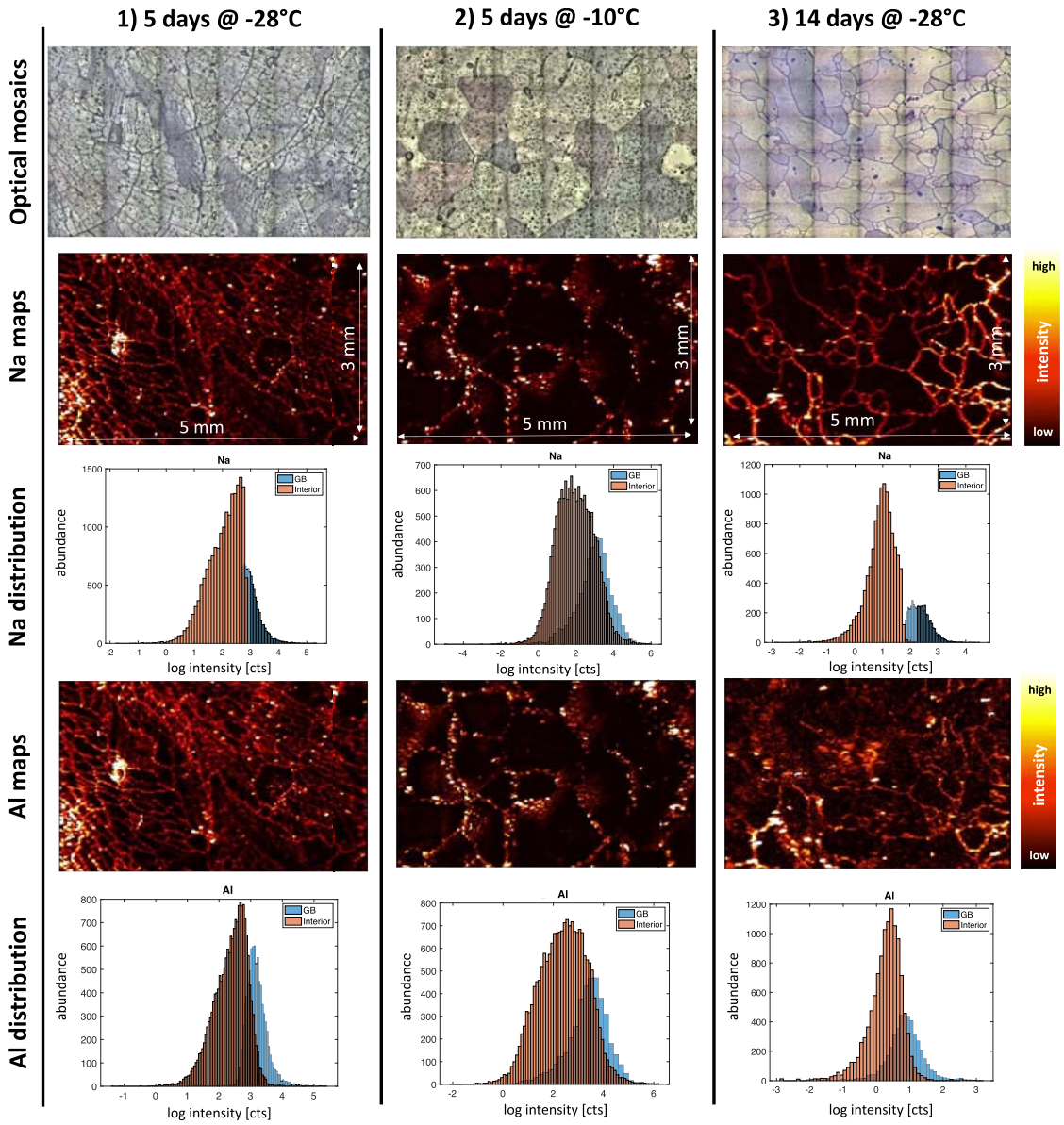


**Figure 4.** Overview of impurity distribution from basic grain growth experiments with method C. Shown are exemplary intensity maps for Na and Al recorded with a 20 µm spot. Ice was made from a 1 ppm standard solution. Histograms for grain boundary and grain interior intensities are also shown. Samples were aged for 5 days at –(28 ± 1)°C (column 1), for 5 days at –(10 ± 2)°C (column 2), and for 14 days at –(28 ± 1)°C (column 3).

illustrated in Figure 1c, three different cases of evolution are displayed. Column 1 shows results obtained from ice stored for 5 days at −(28 ± 1)°C. The visual surface features abundant small grains. The comparatively higher intensities at grain boundaries but still-present signals in grain interiors can be seen in the chemical maps and in the histograms showing the respective intensity distribution for the two regions separately (Figure 4). Column 2 shows the result for ice stored for the same amount of time, 5 days, but aged at a higher temperature of −(10 ± 2)°C. In this case, the optical mosaic shows larger, mm-sized grains. The different color or brightness of grains is likely connected to the birefringent nature of ice, the camera quality, the slightly polarized light source of the instrument, and the fact that some light is reflected from the aluminum block supporting the composite slide. Also, in this case (column 2), higher intensities occur at grain boundaries, but some signals remain distributed in the grain interior. Column 3 shows the case of ice aged for 14 days at −28°C. This sample features grains of variable sizes (below 1 mm to several mm). For Na, most of the high intensities come from the grain boundaries, while in the case of Al, more distributed intensities remain also in the grain interiors.

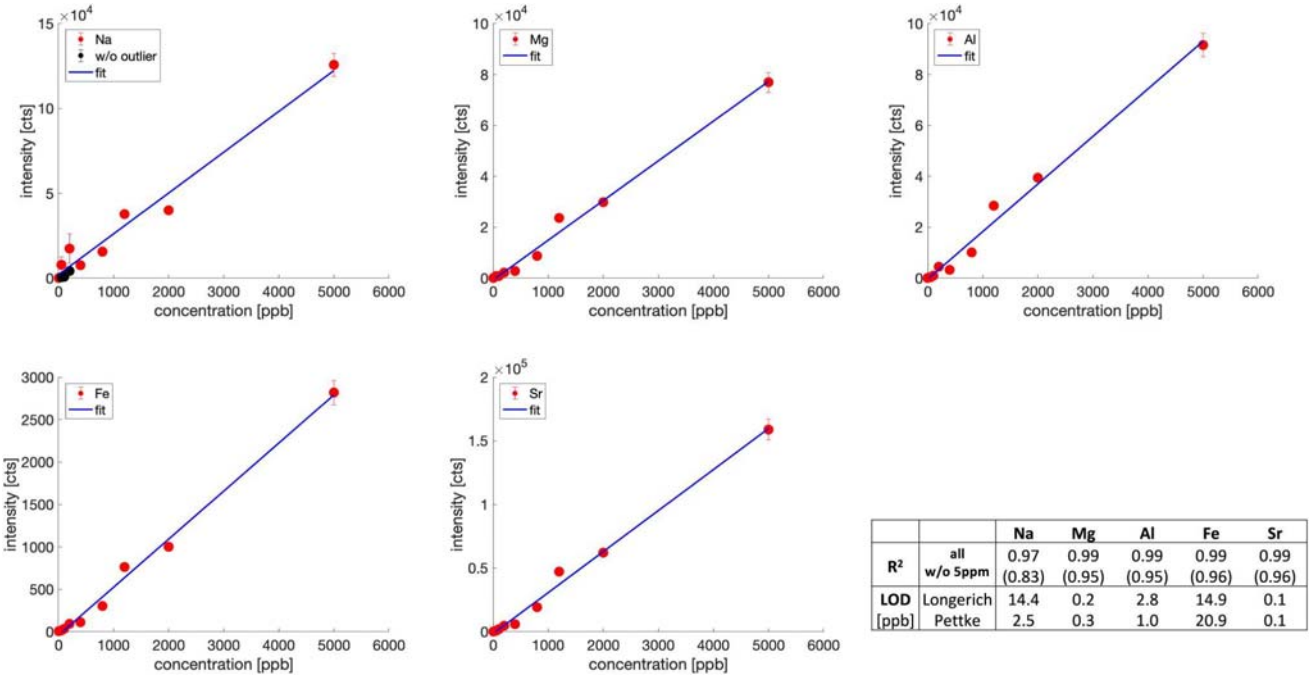


| | | Na | Mg | Al | Fe | Sr |
|---|---|---|---|---|---|---|
| $R^2$ | all | 0.97 | 0.99 | 0.99 | 0.99 | 0.99 |
| | w/o 5ppm | (0.83) | (0.95) | (0.95) | (0.96) | (0.96) |
| LOD [ppb] | Longerich | 14.4 | 0.2 | 2.8 | 14.9 | 0.1 |
| | Pettke | 2.5 | 0.3 | 1.0 | 20.9 | 0.1 |

**Figure 5.** Calibration experiment based on method B. The red points show the mean intensity values (1 sigma error bars) against the concentration in the standard solution used to prepare the respective drops. Black dots for low Na concentrations are outlier-corrected values. Linear regression (blue) reveals high linearity; $R^2$ values are reported in the table. Bracketed values correspond to $R^2$ values calculated without the highest concentration value. The table also reports limits of detection following Longerich et al. (1996) and Pettke et al. (2012) in brackets.

### 3.3. Calibration and Quantitative Analysis of Ice Core Maps

Figure 5 shows the results of a typical calibration experiment using method B. Mean values for intensities obtained within the drop areas are plotted against the respective concentrations of the standard solution along with a linear regression. There is generally a high degree of linearity, with an average $R^2$ value of 0.987. The linearity is still good if the highest concentration is excluded ($R^2$ average 0.931). The individual values $R^2$ are included in Figure 5. The lower $R^2$ values for Na are due to the higher variability in mean intensities for low-concentration standards. Closer inspection showed this goes back to a few spurious pixels of high intensities close to the drop edges. These pixels can result from splattering when ablating the surrounding composite substrate (seen visually on the live image of the laser camera) but can be corrected by the removal of isolated pixels of anomalous high intensity (black points in Figure 3 correspond to the corrected averages). Other elements are affected less or not at all by this splattering (cf. Mg shown in Figure 2). The corresponding limits of detection (LOD) were calculated using HDIP by considering the 3-sigma level of the background (gas blank) following Longerich et al. (1996), as well as by using the approach by Pettke et al. (2012), which is based on Poisson statistics and reports the minimum detectable value with 5% probability for false detection. The respective values are shown in Figure 5.

Using the slope of the calibration line, net intensities obtained in the ice core maps are converted to concentrations, resulting in the quantitative maps shown in Figures 6–9. Fe remains below LOD for all maps except EGRIP3316. The elements show the previously observed localization at grain boundaries, while most of the grain interiors fall below the LOD. Especially in Greenland glacial ice, Al is also visible in dispersed clusters, likely corresponding to mineral dust particles. Concentration ranges are generally higher in glacial versus Holocene samples and higher in Greenland versus Antarctic ice. Na shows the highest concentrations reaching the ppm level within some localized sections of grain boundaries in Greenland ice. On the other hand, Sr only reaches a few ppb, even in the Greenland glacial samples. The lowest concentrations are observed in the EDC Holocene sample, where only Na and Mg remain above the LOD. Using watershed segmentation on the grain boundary network visible in the Na maps, mean values for concentrations within the grain boundaries, the grain interior and the entire map have been calculated (Table 2).

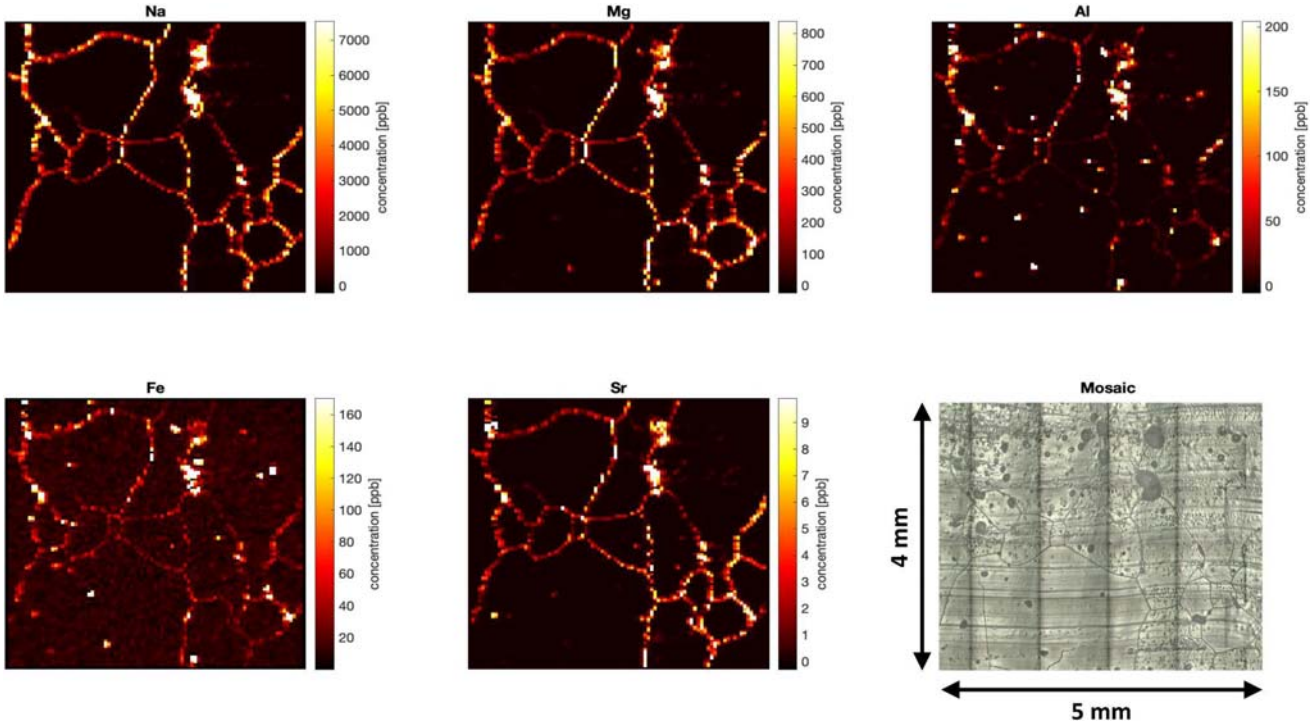


**Figure 6.** Calibrated maps (40 μm spot size) of elemental concentrations in EGRIP3316 glacial ice and optical image of the same area. Map size 5 × 4 mm.

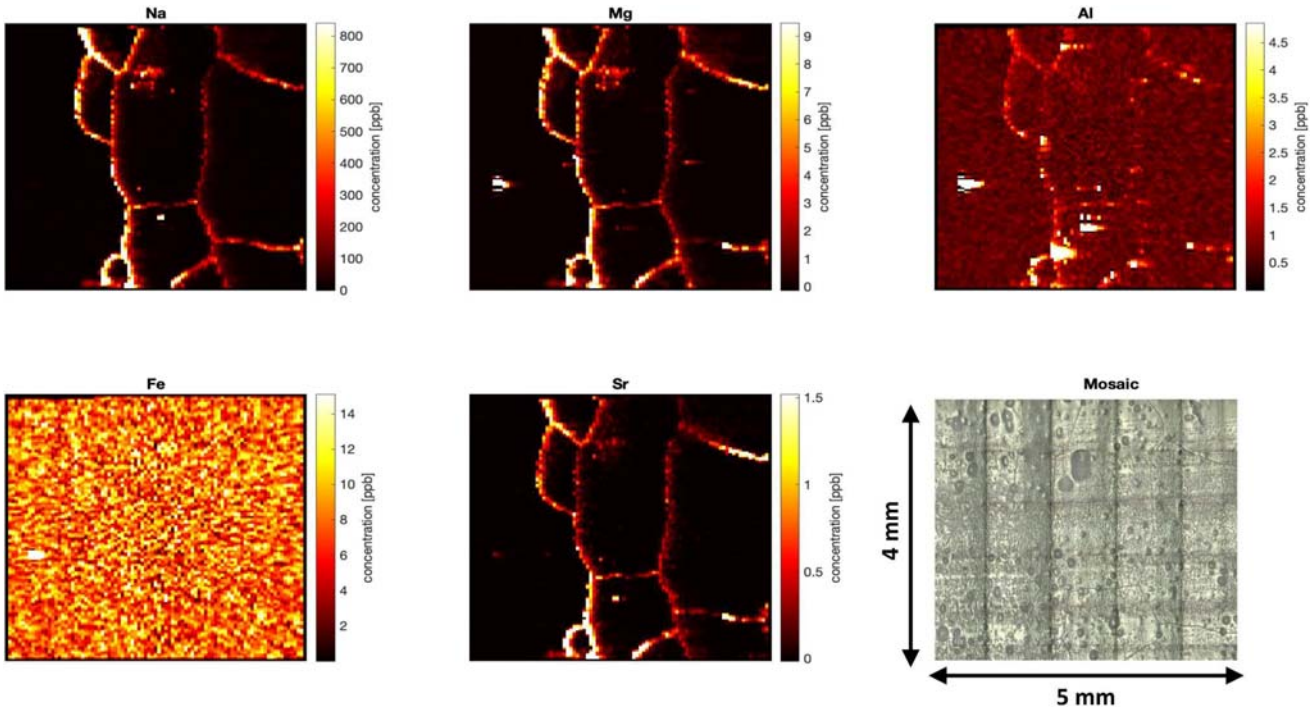


**Figure 7.** Calibrated maps (40 μm spot size) of elemental concentrations in EDC1994 glacial ice and optical image of the same area. Map size 5 × 4 mm.

10.1029/2023GC011425

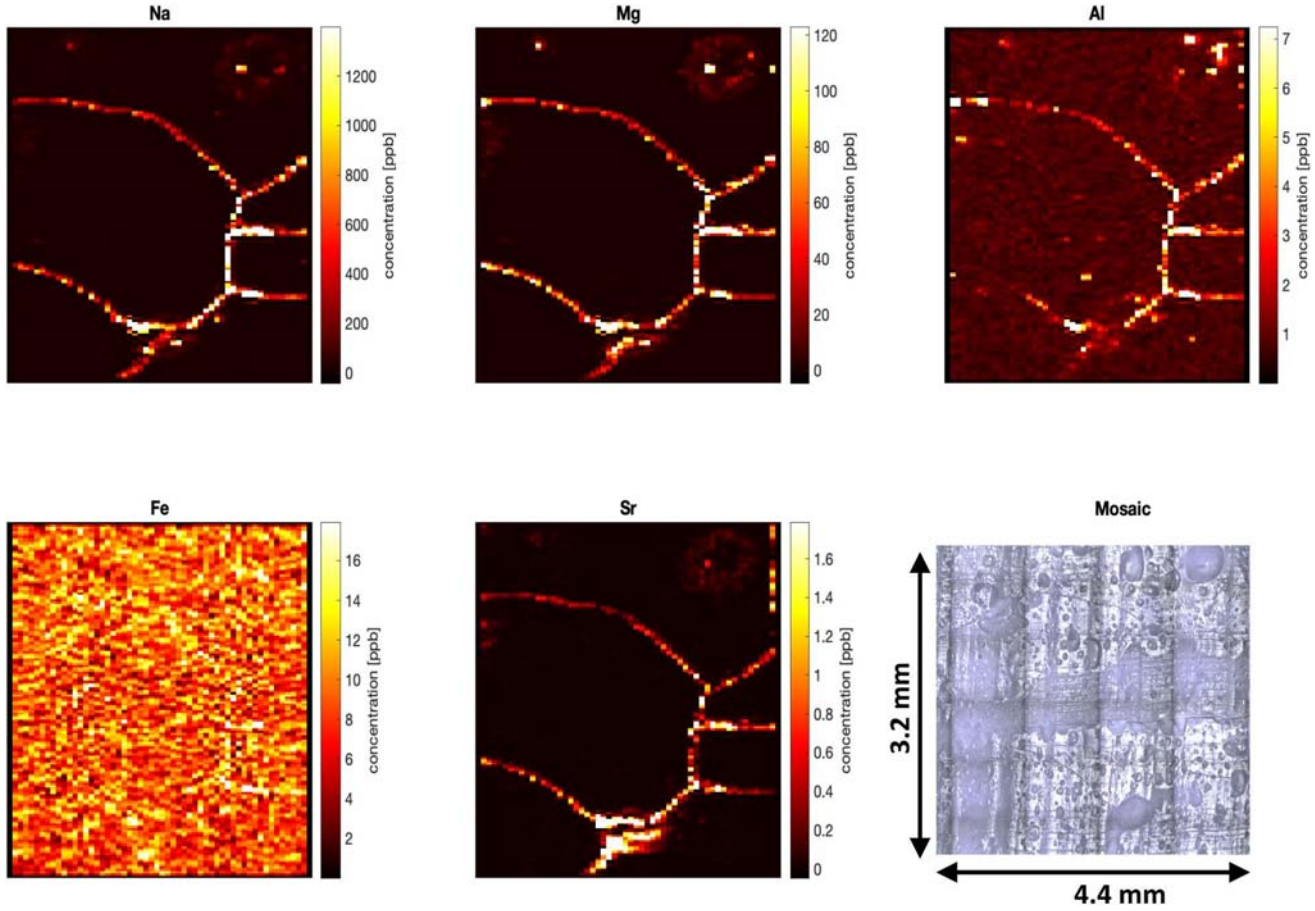


**Figure 8.** Calibrated maps (40 μm spot size) of elemental concentrations in EGRIP253 Holocene ice and optical image of the same area. Map size: 4.4 × 3.2 mm.

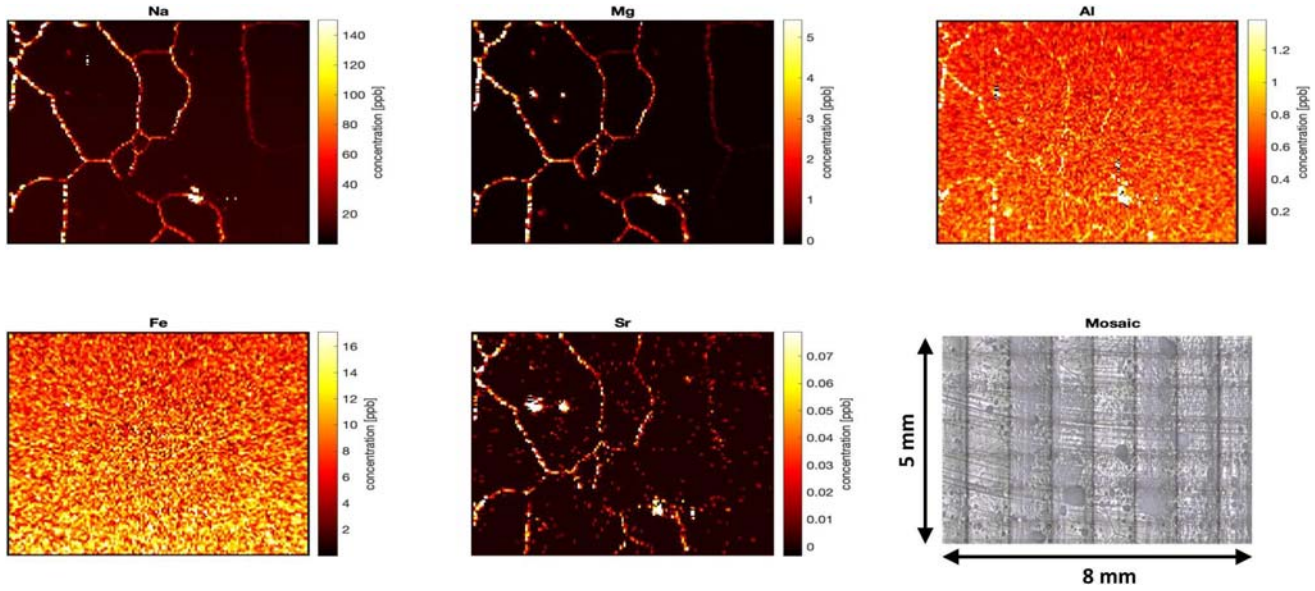


**Figure 9.** Calibrated maps (40 μm spot size) of elemental concentrations in EDC514 Holocene ice and optical image of the same area. Map size: 8 × 5 mm.

**Table 2**
*Average Concentration in Grain Boundaries, Grain Interiors, and in Full Maps for the Data Shown in Figures 6–9*

| | | Na (ppb) | Mg (ppb) | Al (ppb) | Fe (ppb) | Sr (ppb) |
|---|---|---|---|---|---|---|
| Glacial | | | | | | |
| GB | EGRIP | 3,001 ± 475 | 312 ± 31 | 45 ± 6 | 49 ± 6 | 3.0 ± 0.3 |
| | EDC | 352 ± 56 | 3.9 ± 0.4 | (1.6 ± 0.2) | <LOD | 0.50 ± 0.04 |
| Interior | EGRIP | 34 ± 5 | 6 ± 1 | 5 ± 1 | (15 ± 1) | 0.27 ± 0.04 |
| | EDC | 20 ± 3 | 0.4 ± 0.1 | (1.1 ± 0.2) | <LOD | <LOD |
| Full map | EGRIP | 436 ± 70 | 47 ± 5 | 11 ± 1 | (20 ± 2) | 0.59 ± 0.06 |
| | EDC | 54 ± 9 | 0.8 ± 0.1 | (1.1 ± 0.2) | <LOD | <LOD |
| Holocene | | | | | | |
| GB | EGRIP | 955 ± 184 | 79 ± 12 | 4 ± 1 | <LOD | 1.0 ± 0.1 |
| | EDC | 84 ± 14 | 3.0 ± 0.4 | (1.0 ± 0.1) | <LOD | (0.03 ± 0.01) |
| Interior | EGRIP | 24 ± 4 | 2.1 ± 0.3 | 0.9 ± 0.1 | <LOD | <LOD |
| | EDC | 10 ± 2 | <LOD | <LOD | <LOD | <LOD |
| Full map | EGRIP | 78 ± 14 | 6 ± 1 | (1.0 ± 0.1) | <LOD | (0.1 ± 0.01) |
| | EDC | 15 ± 2 | (0.28 ± 0.04) | <LOD | <LOD | <LOD |

*Note*. Bracketed values refer to values close to the LOD but with still visible signals in the maps and should serve only as a tentative indicator of the concentration level.

## 4. Discussion

### 4.1. New Methods for Making Artificial Ice Standards for Imaging Applications

To enable quantitative imaging in ice core samples, the present study developed and evaluated three methods to manufacture artificial ice standards. Compared to the previous studies preparing ice standards from milliliters of solution at a time (Della Lunga et al., 2017; Reinhardt et al., 2001), here the frozen sample volume was significantly reduced to around 85, 0.5 and 360 µL for methods A, B, and C, respectively. However, our new high-resolution (tens of microns) two-dimensional scope for imaging makes the direct comparison not straightforward: With 200–300 µm spot sizes, a sufficient degree of homogeneity in the order of 10%–15% RSD was achieved in the previous studies, where long washout (7 min; Reinhardt et al., 2001) or a "squid" device (Della Lunga et al., 2014, 2017) aided with signal stability. Up to now, it remains unclear how a full matrix-matched calibration can be achieved for state-of-the-art ice core imaging, where fast washout (in the range of a few 10 ms) and small spot sizes (20–40 µm) are indispensable. This is because the high-resolution also means that heterogeneities on the scale of tens of µm become relevant. As expected, fast freezing is beneficial, but reducing the sample volume also plays an important role in achieving homogeneity at the 10 µm scale: RSD values in methods A and B are comparable to those achieved in the previous studies. RSD values for method C (with the largest volume) are higher at 20–40 µm resolution. At coarser resolution, however, the apparent homogeneity increases. To illustrate this effect, we used the approach developed by Bohleber et al. (2021): Starting with a map at 20 µm resolution, we simulated maps obtained with a stepwise increase in spot size and washout time (Figure S2 in Supporting Information S1). The homogeneity was found to increase to reach an RSD of less than 20% at a resolution of a few hundred µm. This also indicates why, although the previous studies froze several mL of standard solution at a time, the degree of homogeneity was also sufficient for the comparatively large spot and washout times used.

With a growing number of laboratories investing in LA-ICP-MS ice core imaging, each method presented in this study may have particular merits for particular instrumental setups and target samples. Moreover, ice standards prepared from the same solution and via the same method may also offer a reproducible approach to inter-laboratory comparisons. In this context, each method has the following specific strengths and weaknesses.

Method A allows decontamination by scraping, analogous to the procedure used to decontaminate ice core samples prior to analysis. The resulting surfaces are flat, allowing imaging over maximum areas of about $2 \times 2$ mm$^2$. The fact that the sample is comparatively thick means that high fluences and large spots can be applied if needed without ablating part of the housing material containing samples. For this reason, method A was our

choice to conduct the fluence experiments shown in Figure 3. The method requires a dedicated holder, the availability of liquid $N_2$ and, ideally, a scraping device.

Method B employs the smallest volume and appears to achieve a slightly better degree of homogeneity than method A. The remaining degree of small-scale heterogeneity illustrated in Figure 2 is likely impacted by the presence of small air bubbles with comparatively reduced impurity levels (e.g., Figure 1B3). Additional strengths of method B are the comparatively fast sample preparation (about 30 min) and the number of samples not being restricted by a holder or mold chambers. For this reason, it became our first choice for performing calibration experiments, with method A being an alternative. Albeit now at the scale of tens of microns, the degree of linearity achieved is comparable to the previous approaches (Della Lunga et al., 2017; Reinhardt et al., 2001). The strength of the small volume also entails an experimental challenge: During analysis, if the temperature of the cooling fluid and hence the underlying surface is not cold enough, sublimation within the He atmosphere of the ablation chamber occurs and leads to fast degradation of the droplets. For this reason, the drops should be measured right after insertion into the ablation chamber. The impact of sublimation may also impose practical lower limits on the volume of the droplets, c.f. a few 100 pL used by Schweikert et al. (2022). As mentioned above, the ablation settings used here do not allow complete consumption of the drops within one ablation run. At the same time, it was observed that the splattering effect from the substrate became more impactful for sections that had been previously ablatedThis posed a special bias for low-concentration samples, and thus the combination of multiple runs was not feasible in practice.

Method C has the largest volume and the largest degree of heterogeneity, illustrating the benefit of reduced sample volume. If a mold with several chambers is used, the simultaneous preparation of different concentration levels is possible. For a calibration experiment, comparatively large areas should be ablated to capture the degree of homogeneity. The ice prepared using this method does not withstand combinations of large fluences and large spots, for example, $>4$ J cm$^{-2}$ and $>40$ µm. In our investigation, the clear strength of this method lies in a different area: the investigation of impurity displacement in ice.

### 4.2. Insights Into the Origin of Impurity Localization in Glacier Ice

While glacier ice grain size evolution with depth is well documented by measurements and modeling, the exact mechanisms of the interplay between processes, such as grain growth and impurity localization in ice, are still debated (e.g., Alley et al., 1986; Stoll, Eichler, Hörhold, Shigeyama, & Weikusat, 2021). Although it is widely accepted that most impurities are incompatible with the ice lattice and that grain growth and various recrystallization mechanisms can thus lead to expulsion and subsequent localization of impurities at grain boundaries, the co-evolution of impurities and ice microstructure is rarely studied contextually (e.g., the overviews provided by Della Lunga et al., 2014; Stoll, Eichler, Hörhold, Shigeyama, & Weikusat, 2021 and references therein). However, the interaction between grain growth and impurities is expected to be far more complex than a simple expulsion, especially for particulate matter, and can involve pinning or dragging effects (Alley et al., 1986; Stoll, Eichler, Hörhold, Shigeyama, & Weikusat, 2021). The ice-impurity interplay marks an important frontier in understanding glacier ice at the micro-scale, with important impacts on macroscopic properties such as ice flow and deformation and the integrity of paleoclimatic signals. The storage and aging experiments conducted here (method C) provide a direct observation of grain growth-induced impurity displacement in laboratory ice, for the first time using chemical imaging in concert with visual analysis. This is an important complement to previous laboratory studies, which mainly focused on the visual domain only (Kubo et al., 2009). The results confirm the suspected role of grain growth as the main driver of the impurity localization at grain boundaries, as seen through LA-ICP-MS imaging in intermediate depths (Bohleber et al., 2021) and to a lesser degree in firn and shallow ice (Stoll, Bohleber, et al., 2023). The differences in aged Na and Al distribution in column 3 may be explained by different degrees of mobility, especially if Al features a significant particulate fraction (see SP-ICP-TOFMS results below). We also find clear evidence for temperature to be a decisive factor in the time evolution of the grain formation, as is expected by theoretical considerations and observations (e.g., Durand et al., 2006; Gow, 1969). Using method C for aging artificial ice under variable impurity load and temperature conditions opens the way for various follow-up experiments exploring the interplay between the ice matrix and impurities, especially particles, in further detail. The transfer between artificial ice and glacier ice is not straightforward, considering glacier ice under natural conditions "ages" under high hydrostatic pressure (being compressed by up to 4,000 m ice thickness) and, more importantly, over a time scale (up to several 100,000 years, millions in some instances) that is impossible to reproduce in the laboratory. However, it may be possible to use the laboratory to

arrive at a similar configuration through a much shorter evolution, for example, aided by higher temperature. This approach could provide a reference for comparison between meltwater bulk concentration and quantitative maps by comparing aged mold standards with ice core samples that show similar signal intensities at grain boundaries and grain interior. The corresponding bulk concentration is known based on the standard sample used. Ultimately, it is clear that method C shows considerable future potential. However, the large experimental effort required for a thorough investigation of these applications warrants separate dedicated studies.

### 4.3. Quantitative Impurity Imaging on Ice Cores

Method B allows intensity maps obtained from LA-ICP-MS imaging at a resolution of 40 μm to be reliably converted to concentration maps using matrix-matched standards. The calibrated LA-ICP-MS maps (Figures 6–9) show that while a similar degree of localization at grain boundaries is found in all samples, concentration levels vary distinctly, with higher concentrations in glacial periods and Greenland samples and lower concentrations in interglacial periods and samples from central Antarctica. For further quantification, the mean concentration for the grain boundaries, the grain interiors, and the average of the entire image (Table 2) were calculated separately for each map. Considering Na and Mg, the enrichment at grain boundaries relative to the entire map average is around a factor of 5–7 for glacial ice and 6–13 for Holocene ice. The higher enrichment for the latter comes from having less signal from the grain interiors. In some cases, the grain interiors contribute significantly to the full map average concentrations, which is in agreement with previous studies (Bohleber et al., 2023; Stoll, Westhoff, et al., 2023). Notably, pixels belonging to the grain boundary class make up a considerable fraction of the images, around 7%–8% for Holocene and 11%–16% for glacial samples. Figure 9 (EDC Holocene) suggests that Al signals can still be detected below the LOD of Longerich et al. (1996), arguing for the limits of Pettke et al. (2012) being more realistic in this context. Accordingly, it is now possible to state that the grain interiors are not necessarily free from impurities, but that instrument LODs can provide an upper limit to the concentrations within the signal-free areas.

Uncertainties for the values in Table 2 are derived through error propagation based on the 95% confidence interval in the calibration curve (representing uncertainties associated with the ice standards) and the standard deviation of the mean intensities (representing the spatial variability in the ice), which each contribute generally at a comparable level. For the grain boundary segments and the full image, the uncertainty ranges within typically 10%–14%. In the full maps, the uncertainty at the level of an individual pixel is likely higher, which must be considered when interpreting the maps on that scale. Additional uncertainty can come from misassignments in the segmentation of the grain boundaries, which are difficult to fully quantify. However, the uncertainties of the mean values fall well within the 5%–20% uncertainty envelope reported by Della Lunga et al. (2017) for their calibrated datasets.

Due to the high-resolution nature of these datasets, a comparison with other reference data is fundamentally challenging. Della Lunga et al. (2017) obtained 2D maps by interpolating a raster of spots, with 144 datapoints over 4 × 4 mm from glacial ice from the NGRIP Greenland ice core. The map in Figure 6 showing EGRIP glacial ice is based on 9100 datapoints over 5 × 4 mm. While Al and Fe show levels comparable to Della Lunga et al. (2017), Na and Mg levels are higher by about one order of magnitude. Considering the high degree of localization at grain boundaries for Na and Mg, it is reasonable to explain this difference first and foremost by the higher resolution of the data. Impurity concentrations are strongly variable with time and depth within glacial periods, which plays an additional role. Differences due to the location of the drilling sites are probably negligible as EGRIP ice is situated on the northeast Greenland ice stream, meaning its ice likely originates from the ice divide region close to the NGRIP drill site.

The comparison with concentration measurements from discrete or continuous meltwater samples makes the gap in resolution even greater. While continuous meltwater analysis is typically representative for a 3.5 × 3.5 × 1 cm volume (Breton et al., 2012; Dallmayr et al., 2016), the map averages represent discrete 2D snapshots of a few $mm^2$. Adding to this complex scale gap, typical mean values for impurity concentrations during the Holocene and last glacial period average over long periods with considerable signal variability. Acknowledging this challenging setting, we were able to use the Na bag mean values recently obtained from CFA for EDC (representing approximately 3.5 × 3.5 × 55 cm volume), which showed similar bulk values as the full map averages: Na has a 15 ppb average for EDC bag 513, with a range of 5–33 ppb (one bag away from our sample). Bag 1994 had a Na average of 52 ppb and a range of 27–81 ppb. The full map averages obtained here agree well with this range. At an

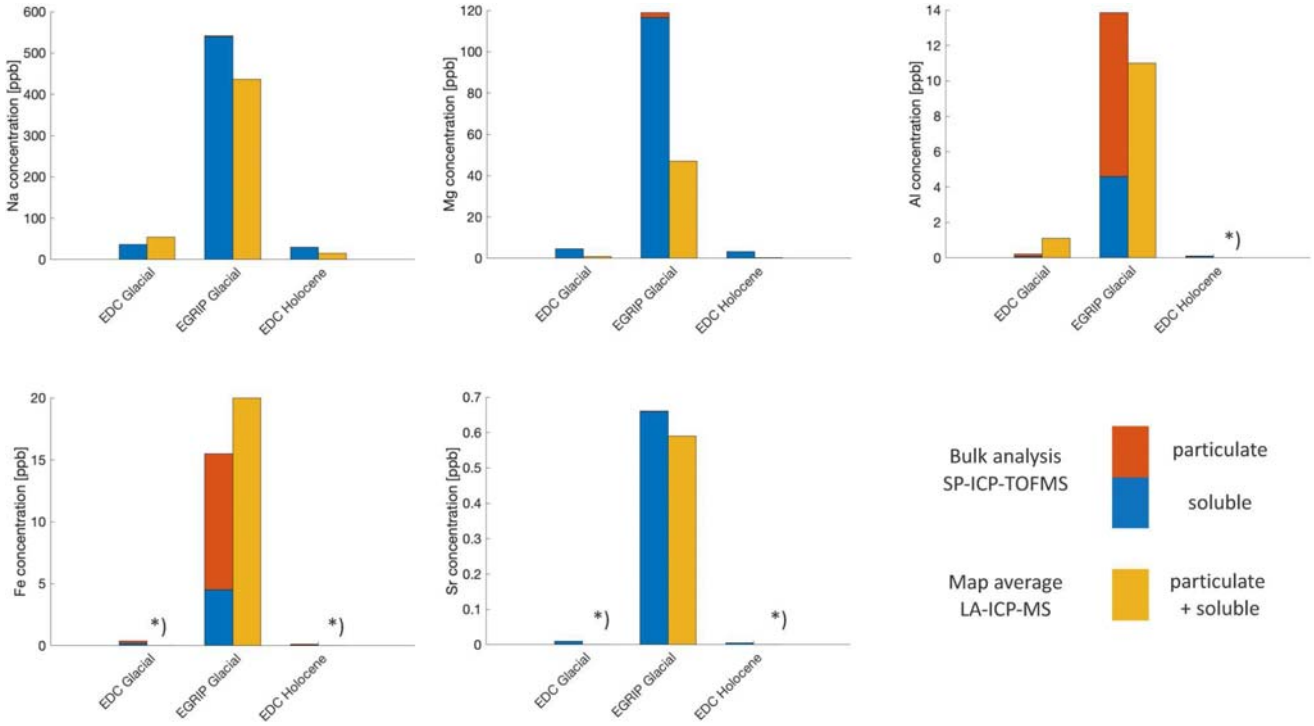


**Figure 10.** Comparison of full-map averages by calibrated LA-ICP-MS with bulk analysis from SP-ICP-TOFMS on samples of the same core. For the liquid bulk analyses, the soluble contribution is marked in blue and the particulate contribution is marked in red.

intermediate level in the scale gap, the discrete samples analyzed by bulk SP-ICP-TOFMS represent bulk volumes of a few mL. Figure 10 shows a comparison with the calibrated full map averages. The values from bulk and laser ablation analysis show the same general trends regarding relative higher and lower concentrations. It is further interesting to note that the EGRIP glacial samples stand out in the bulk SP-ICP-TOFMS analysis by showing a distinct contribution of particles to the overall concentration of Al and Fe, which is consistent with the dispersed particle clusters shown in the respective LA-ICP-MS images, especially for Al.

Regarding a direct comparison of values between the two techniques, the bulk measurements typically lie within a factor of 2 within the LA-ICP-MS averages. One contribution to this difference can stem from the depth-distance among the samples (approx. 50 cm for EDC513 and EDC514). However, the comparison between EDC1994 and EDC1995 bulk values shows that, at least for Na and Mg, the concentrations show minor differences, while Al and Fe (with a stronger insoluble component) show greater spatial variability. It also has to be considered that, on the mm to cm scale geometry of the samples, relative variability in grain size may impact the mean values of impurities highly localized at grain boundaries (e.g., as recently discussed in Ng (2021)). The fact that the bag mean values for Na are very close to the map means would argue that the grain size variability averages out on that scale. Within this context, it becomes evident that more sophisticated techniques for bridging the scale gap need to be developed that specifically take into account the role of impurity localization and grain size variability. Considering the high concentrations observed at the grain boundaries, the broad agreement of the full map averages with bulk measurements is an encouraging result in this framework: It indicates that some linkage could be possible between the scales of LA-ICP-MS maps and bulk meltwater analysis.

Accordingly, the calibrated LA-ICP-MS maps provide important insight for understanding the chemistry of ice cores from the micro-scale to the cm-scale. For each measured elemental species the calibrated maps contain information on (a) the degree of localization at grain boundaries, but also add information on (b) the concentration levels at the grain boundaries and on (c) the concentration levels within grain interiors. Knowing these parameters will be crucial to making meaningful extrapolations to the cm-scale of bulk measurements, in particular when combined with existing data about the ice microstructure coming from optical datasets.

### 4.4. Limitations and Future Work

The maps obtained from Greenland and Antarctic ice show that, even if bulk concentrations may be limited, the concentrations of some impurities like Na can become substantial at the grain boundaries reaching into the ppm range. This may also be the case for other comparatively abundant impurities, such as sulfate, chloride and calcium (Legrand & Mayewski, 1997). It is reasonable to expect that deep ice conditions at for example, the Beyond EPICA Oldest Ice site are characterized by large (cm-sized) grains and a high degree of impurity localization. However, it remains unclear how high the concentrations at grain boundaries in deep warm ice may become and how this impacts the mobility of the impurities, the local pH level at grain boundaries, and the presence of microscopic amounts of liquid water potentially present in veins. Quantitative LA-ICP-MS imaging may provide important insights into investigating such special circumstances. However, fully quantitative analysis may also require further extending the standards' concentration range: Considering the example of Na in Figure 6, concentrations go slightly beyond the calibrated range and must be regarded as an extrapolation. At the same time, we find that extending the calibration range further is a challenge due to the eventual shift to uncontrolled ablation regimes. Reinhardt et al. (2001) used $m/z = 17$ as an internal standard from the ice matrix to evaluate the ablation efficiency. Under the "controlled" ablation regime of UV-LA, the ablated sample volume is too low to resolve the signal of $m/z = 17$ above background, as previously noted by Della Lunga et al. (2017). Although a correction for the ablation efficiency could be possible with $m/z = 17$ and would aid in calibration stability (Mervič et al., 2024), we found that this effect cannot be fully compensated by normalization to the $m/z = 17$ signal. This is possibly due to changes in the aerosol transport for a wider distribution and larger amounts of aerosols being generated, resulting in inefficient or variable collection and transfer of the plume to the ICP-MS. However, it appears that the signal of $m/z = 17$ can be used to detect the transition between controlled and uncontrolled ablation, and we have demonstrated how it is possible to explore the parameter space defined by concentration and ablation conditions. This approach can be adapted to specific experiments on artificial ice samples to provide guidance in finding suitable ablation parameters.

Notably, the impurity signals show a corresponding increase in signal intensity and variability for constant concentration levels for the regions with increased signal in $m/z = 17$ (Figure 3). This effect becomes especially evident for 65 µm spots and concentrations below 1 ppm, showing the impact of increased but variable volume of ablation. Similar effects have been observed recently with gelatin, and any material will likely be affected if high enough fluences and beam sizes are used (Jerše et al., 2022). Notably, detecting this impact of fluence and beam size on image quality is only afforded by high-resolution mapping, that is, not recognized when smoothing devices ("squid" or large volume ablation cells) are used. However, it also has to be noted that a direct transfer of these results from standards to ice core samples is not always possible: For ice core samples, it is mostly possible to operate at fluences of 4–5 J $cm^{-2}$ without necessarily reaching the uncontrolled ablation regime. This is likely, first and foremost, due to the localized nature of impurities in ice core samples versus the comparatively homogenous nature of ice standards changing the ablation characteristics of the ice. It appears that, at higher concentrations, the distributed nature of the impurities in the standards increases the coupling between the ice matrix and the UV-laser—which is otherwise expected to be relatively weak at 193 nm (Warren & Brandt, 2008). Qualitatively, this view would also explain the apparent dependency on spot size, as larger spots simply deliver more total energy per shot. Along these lines, our results show that using smaller spots may partially mitigate the onset of the uncontrolled regime. High repetition rate imaging lasers benefit from faster analysis times and may therefore use smaller spots while analyzing the same or larger area sizes, which is especially needed when imaging large grains in deep ice. As an alternative technological solution, the use of femtosecond lasers may even circumvent this calibration issue for high concentrations altogether.

## 5. Conclusions

Matrix-matched calibrations are a known challenge for LA-ICP-MS, and applications to glacier ice are no exception. Since recent developments in state-of-the-art imaging techniques have changed the paradigm toward fast washout and high repetition rate mapping, LA-ICP-MS ice core analysis has not only completed the step into 2D analysis from 1D analysis but has also increased the resolution by at least one order of magnitude (e.g., from 200 to 20 µm). Consequently, a new approach to calibration had to be developed that provided a sufficient degree of homogeneity. We have presented three different methods and assessed their strengths and weaknesses. Two methods (A and B) are suitable for carrying out external calibration. These methods provide a comparable degree of spatial homogeneity of impurity distribution and linearity in

calibration as reported in previous coarser resolution studies. Limitations arose from changes in ablation behavior for high concentration standards (>10 ppm), and we show how this shift into destructive ablation could be detected by monitoring $m/z = 17$ allowing a dedicated selection of laser parameters. The third method (C) stands out by offering a new method to simulate grain growth induced displacement of impurities, leading to heterogeneous distributions, comparable to that seen in glacier ice samples, with a high degree of localization at grain boundaries for elements such as Na.

Calibrated LA-ICP-MS maps show that while a similar degree of localization at grain boundaries is present in all samples analyzed, the respective impurity levels vary significantly. Concentrations in glacial periods and Greenland are generally higher by up to an order of magnitude as compared to interglacial periods and samples from central Antarctica. With a growing number of laboratories investing in LA-ICP-MS ice core imaging, ice standards may also facilitate inter-laboratory comparisons. Ultimately, adding the quantitative dimension to in-depth comparisons with bulk meltwater data may lead to a new level of insight about the chemical stratigraphy in ice cores across scales, including an important step forward in understanding deep ice conditions.

## Data Availability Statement

The underlying data used for creating the chemical maps in the study are available at zenodo.org via https://doi.org/10.5281/zenodo.10680251 (Bohleber et al., 2024) with license Creative Commons Attribution 4.0 International.

**Acknowledgments**
The authors thank Alessandro Bonetto, Ciprian Stremtan, and Stijn van Malderen for their continued technical support. We thank the Division for Climate and Environmental Physics, University of Bern, for sharing the EDC bag mean values measured using the Bern Continuous Flow Analysis system for comparison. Pascal Bohleber gratefully acknowledges funding from the European Union's Horizon 2020 research and innovation program under the Marie Skłodowska-Curie grant agreement no. 101018266. Nicolas Stoll and Pascal Bohleber gratefully acknowledge funding from the Arctic Research Program of Italy (PRA). The authors would like to acknowledge the Slovenian Research and Innovation Agency (ARIS) for core funding P1-0034. EGRIP is directed and organized by the Centre for Ice and Climate at the Niels Bohr Institute, University of Copenhagen. It is supported by funding agencies and institutions in Denmark (A. P. Møller Foundation, University of Copenhagen), USA (US National Science Foundation, Office of Polar Programs), Germany (Alfred Wegener Institute, Helmholtz Centre for Polar and Marine Research), Japan (National Institute of Polar Research and Arctic Challenge for Sustainability), Norway (University of Bergen and Trond Mohn Foundation), Switzerland (Swiss National Science Foundation), France (French Polar Institute Paul-Emile Victor, Institute for Geosciences and Environmental research), Canada (University of Manitoba), and China (Chinese Academy of Sciences and Beijing Normal University). The project has received funding from the European Union's Horizon 2020 research and innovation programme under grant agreement No. 815384 (Oldest Ice Core). It is supported by national partners and funding agencies in Belgium, Denmark, France, Germany, Italy, Norway, Sweden, Switzerland, The Netherlands and the United Kingdom. Logistic support is mainly provided by ENEA and IPEV through the Concordia Station system. The opinions expressed and arguments employed herein do not necessarily reflect the official views of the European Union funding agency or other national funding bodies. This is Beyond EPICA publication number 36.

## References

Alley, R. B., Perepezko, J. H., & Bentley, C. R. (1986). Grain growth in polar ice: I. Theory. *Journal of Glaciology*, *32*(112), 415–424. https://doi.org/10.3189/S0022143000012120

Baccolo, G., Delmonte, B., Di Stefano, E., Cibin, G., Crotti, I., Frezzotti, M., et al. (2021). Deep ice as a geochemical reactor: Insights from iron speciation and mineralogy of dust in the Talos Dome ice core (East Antarctica). *The Cryosphere*, *15*(10), 4807–4822. https://doi.org/10.5194/tc-15-4807-2021

Bohleber, P., Larkman, P., Stoll, N., Clases, D., Gonzalez de Vega, R., Šala, M., et al. (2024). Supporting data for manuscript "Quantitative insights on impurities in ice cores at the micro-scale from calibrated LA-ICP-MS imaging" (1.0) [Dataset]. *Zenodo*. https://doi.org/10.5281/zenodo.10680251

Bohleber, P., Roman, M., Šala, M., & Barbante, C. (2020). Imaging the impurity distribution in glacier ice cores with LA-ICP-MS. *Journal of Analytical Atomic Spectrometry*, *35*(10), 2204–2212. https://doi.org/10.1039/d0ja00170h

Bohleber, P., Roman, M., Šala, M., Delmonte, B., Stenni, B., & Barbante, C. (2021). Two-dimensional impurity imaging in deep Antarctic ice cores: Snapshots of three climatic periods and implications for high-resolution signal interpretation. *The Cryosphere*, *15*(7), 3523–3538. https://doi.org/10.5194/tc-15-3523-2021

Bohleber, P., Stoll, N., Rittner, M., Roman, M., Weikusat, I., & Barbante, C. (2023). Geochemical characterization of insoluble particle clusters in ice cores using two-dimensional impurity imaging. *Geochemistry, Geophysics, Geosystems*, *24*(2), e2022GC010595. https://doi.org/10.1029/2022gc010595

Breton, D. J., Koffman, B. G., Kurbatov, A. V., Kreutz, K. J., & Hamilton, G. S. (2012). Quantifying signal dispersion in a hybrid ice core melting system. *Environmental Science & Technology*, *46*(21), 11922–11928. https://doi.org/10.1021/es302041k

Brook, E. J., Wolff, E., Dahl-Jensen, D., Fischer, H., & Steig, E. J. (2006). The future of ice coring: International partnerships in ice core sciences (IPICS). *PAGES News*, *14*(1), 6–10. https://doi.org/10.22498/pages.14.1.6

Dallmayr, R., Goto-Azuma, K., Kjaer, H. A., Azuma, N., Takata, M., Schüpbach, S., & Hirabayashi, M. (2016). A high-resolution continuous flow analysis system for polar ice cores. *Bulletin of Glaciological Research*, *34*(0), 11–20. https://doi.org/10.5331/bgr.16r03

Della Lunga, D., Müller, W., Rasmussen, S. O., & Svensson, A. (2014). Location of cation impurities in NGRIP deep ice revealed by cryo-cell UV-laser-ablation ICPMS. *Journal of Glaciology*, *60*(223), 970–988. https://doi.org/10.3189/2014JoG13J199

Della Lunga, D., Müller, W., Rasmussen, S. O., Svensson, A., & Vallelonga, P. (2017). Calibrated cryo-cell UV-LA-ICPMS elemental concentrations from the NGRIP ice core reveal abrupt, sub-annual variability in dust across the GI-21.2 interstadial period. *The Cryosphere*, *11*(3), 1297–1309. https://doi.org/10.5194/tc-11-1297-2017

Durand, G., Weiss, J., Lipenkov, V., Barnola, J. M., Krinner, G., Parrenin, F., et al. (2006). Effect of impurities on grain growth in cold ice sheets. *Journal of Geophysical Research*, *111*(F1), F01015. https://doi.org/10.1029/2005jf000320

Fischer, H., Blunier, T., & Mulvaney, R. (2021). Ice cores: Archive of the climate system. In *Glaciers and ice sheets in the climate system* (pp. 279–325). Springer.

Fischer, H., Severinghaus, J., Brook, E., Wolff, E., Albert, M., Alemany, O., et al. (2013). Where to find 1.5 million yr old ice for the IPICS "Oldest-Ice" ice core. *Climate of the Past*, *9*(6), 2489–2505. https://doi.org/10.5194/cp-9-2489-2013

Gerber, T. A., Hvidberg, C. S., Rasmussen, S. O., Franke, S., Sinnl, G., Grinsted, A., et al. (2021). Upstream flow effects revealed in the EastGRIP ice core using Monte Carlo inversion of a two-dimensional ice-flow model. *The Cryosphere*, *15*(8), 3655–3679. https://doi.org/10.5194/tc-15-3655-2021

Gow, A. J. (1969). On the rates of growth of grains and crystals in South Polar firn. *Journal of Glaciology*, *8*(53), 241–252. https://doi.org/10.1017/s0022143000031233

Jerše, A., Mervič, K., van Elteren, J. T., Šelih, V. S., & Šala, M. (2022). Quantification anomalies in single pulse LA-ICP-MS analysis associated with laser fluence and beam size. *Analyst*, *147*(23), 5293–5299. https://doi.org/10.1039/d2an01172g

Kaufmann, P. R., Federer, U., Hutterli, M. A., Bigler, M., Schüpbach, S., Ruth, U., et al. (2008). An improved continuous flow analysis system for high-resolution field measurements on ice cores. *Environmental Science & Technology*, *42*(21), 8044–8050. https://doi.org/10.1021/es8007722

Kubo, T., Nakata, H., & Kato, T. (2009). Effects of insoluble particles on grain growth in polycrystalline ice: Implications for rheology of ice shells of icy satellites. *Journal of Mineralogical and Petrological Sciences*, *104*(5), 301–306. https://doi.org/10.2465/jmps.090622e

Lambert, F., Delmonte, B., Petit, J. R., Bigler, M., Kaufmann, P. R., Hutterli, M. A., et al. (2008). Dust - Climate couplings over the past 800,000 years from the EPICA Dome C ice core. *Nature*, *452*(7187), 616–619. https://doi.org/10.1038/nature06763

Legrand, M., & Mayewski, P. (1997). Glaciochemistry of polar ice cores: A review. *Reviews of Geophysics*, *35*(3), 219–243. https://doi.org/10.1029/96rg03527

Lilien, D. A., Steinhage, D., Taylor, D., Parrenin, F., Ritz, C., Mulvaney, R., et al. (2021). Brief communication: New radar constraints support presence of ice older than 1.5 Myr at Little Dome C. *The Cryosphere*, *15*(4), 1881–1888. https://doi.org/10.5194/tc-15-1881-2021

Longerich, H. P., Jackson, S. E., & Günther, D. (1996). Laser ablation inductively coupled plasma mass spectrometric transient signal data acquisition and analyte concentration calculation. *Journal of Analytical Atomic Spectrometry*, *11*(9), 899–904. https://doi.org/10.1039/JA9961100899

McConnell, J. R., Lamorey, G. W., Lambert, S. W., & Taylor, K. C. (2002). Continuous ice-core chemical analyses using inductively coupled plasma mass spectrometry. *Environmental Science & Technology*, *36*(1), 7–11. https://doi.org/10.1021/es011088z

Mervič, K., van Elteren, J. T., Bele, M., & Šala, M. (2024). Utilizing ablation volume for calibration in LA-ICP-MS mapping to address variations in ablation rates within and between matrices. *Talanta*, *269*, 125379. https://doi.org/10.1016/j.talanta.2023.125379

Mojtabavi, S., Wilhelms, F., Cook, E., Davies, S., Sinnl, G., Skov Jensen, M., et al. (2020). A first chronology for the East Greenland Ice-core Project (EGRIP) over the Holocene and last glacial termination. *Climate of the Past*, *16*(6), 2359–2380. https://doi.org/10.5194/cp-16-2359-2020

Müller, W., Shelley, J. M. G., & Rasmussen, S. O. (2011). Direct chemical analysis of frozen ice cores by UV-laser ablation ICPMS. *Journal of Analytical Atomic Spectrometry*, *26*(12), 2391–2395. https://doi.org/10.1039/c1ja10242g

Ng, F. S. L. (2021). Pervasive diffusion of climate signals recorded in ice-vein ionic impurities. *The Cryosphere*, *15*(4), 1787–1810. https://doi.org/10.5194/tc-15-1787-2021

Parrenin, F., Barnola, J. M., Beer, J., Blunier, T., Castellano, E., Chappellaz, J., et al. (2007). The EDC3 chronology for the EPICA Dome C ice core. *Climate of the Past*, *3*(3), 485–497. https://doi.org/10.5194/cp-3-485-2007

Pettke, T., Oberli, F., Audétat, A., Guillong, M., Simon, A. C., Hanley, J. J., & Klemm, L. M. (2012). Recent developments in element concentration and isotope ratio analysis of individual fluid inclusions by laser ablation single and multiple collector ICP-MS. *Ore Geology Reviews*, *44*, 10–38. https://doi.org/10.1016/j.oregeorev.2011.11.001

Reinhardt, H., Kriews, M., Miller, H., Schrems, O., Lüdke, C., Hoffmann, E., & Skole, J. (2001). Laser ablation inductively coupled plasma mass spectrometry: A new tool for trace element analysis in ice cores. *Fresenius' Journal of Analytical Chemistry*, *370*(5), 629–636. https://doi.org/10.1007/s002160100853

Rempel, A. W., Waddington, E. D., Wettlaufer, J. S., & Worster, M. G. (2001). Possible displacement of the climate signal in ancient ice by premelting and anomalous diffusion. *Nature*, *411*(6837), 568–571. https://doi.org/10.1038/35079043

Röthlisberger, R., Bigler, M., Hutterli, M., Sommer, S., Stauffer, B., Junghans, H. G., & Wagenbach, D. (2000). Technique for continuous high-resolution analysis of trace substances in firn and ice cores. *Environmental Science & Technology*, *34*(2), 338–342. https://doi.org/10.1021/es9907055

Sacré, P. Y., Lebrun, P., Chavez, P. F., De Bleye, C., Netchacovitch, L., Rozet, E., et al. (2014). A new criterion to assess distributional homogeneity in hyperspectral images of solid pharmaceutical dosage forms. *Analytica Chimica Acta*, *818*, 7–14. https://doi.org/10.1016/j.aca.2014.02.014

Schweikert, A., Theiner, S., Šala, M., Vician, P., Berger, W., Keppler, B. K., & Koellensperger, G. (2022). Quantification in bioimaging by LA-ICPMS-Evaluation of isotope dilution and standard addition enabled by micro-droplets. *Analytica Chimica Acta*, *1223*, 340200. https://doi.org/10.1016/j.aca.2022.340200

Sneed, S. B., Mayewski, P. A., Sayre, W. G., Handley, M. J., Kurbatov, A. V., Taylor, K. C., et al. (2015). New LA-ICP-MS cryocell and calibration technique for sub-millimeter analysis of ice cores. *Journal of Glaciology*, *61*(226), 233–242. https://doi.org/10.3189/2015jog14j139

Spaulding, N. E., Sneed, S. B., Handley, M. J., Bohleber, P., Kurbatov, A. V., Pearce, N. J., et al. (2017). A new multielement method for LA-ICP-MS data acquisition from glacier ice cores. *Environmental Science & Technology*, *51*(22), 13282–13287. https://doi.org/10.1021/acs.est.7b03950

Stoll, N., Bohleber, P., Dallmayr, R., Wilhelms, F., Barbante, C., & Weikusat, I. (2023). The new frontier of microstructural impurity research in polar ice. *Annals of Glaciology*, 1–4. https://doi.org/10.1017/aog.2023.61

Stoll, N., Eichler, J., Hörhold, M., Erhardt, T., Jensen, C., & Weikusat, I. (2021). Microstructure, micro-inclusions, and mineralogy along the EGRIP ice core -- Part 1: Localisation of inclusions and deformation patterns. *The Cryosphere*, *15*(12), 5717–5737. https://doi.org/10.5194/tc-15-5717-2021

Stoll, N., Eichler, J., Hörhold, M., Shigeyama, W., & Weikusat, I. (2021). A review of the microstructural location of impurities in polar ice and their impacts on deformation. *Frontiers in Earth Science*, *8*, 658. https://doi.org/10.3389/feart.2020.615613

Stoll, N., Westhoff, J., Bohleber, P., Svensson, A., Dahl-Jensen, D., Barbante, C., & Weikusat, I. (2023). Chemical and visual characterisation of EGRIP glacial ice and cloudy bands within. *The Cryosphere*, *17*(5), 2021–2043. https://doi.org/10.5194/tc-17-2021-2023

Traversi, R., Becagli, S., Castellano, E., Marino, F., Rugi, F., Severi, M., et al. (2009). Sulfate spikes in the deep layers of EPICA-Dome C ice core: Evidence of glaciological artifacts. *Environmental science & technology*, *43*(23), 8737–8743. https://doi.org/10.1021/es901426y

van Elteren, J. T., Metarapi, D., Šala, M., Šelih, V. S., & Stremtan, C. C. (2020). Fine-tuning of LA-ICP-QMS conditions for elemental mapping. *Journal of Analytical Atomic Spectrometry*, *35*(11), 2494–2497. https://doi.org/10.1039/d0ja00322k

Warren, S. G., & Brandt, R. E. (2008). Optical constants of ice from the ultraviolet to the microwave: A revised compilation. *Journal of Geophysical Research*, *113*(D14), D14220. https://doi.org/10.1029/2007jd009744

Westerhausen, M. T., Lockwood, T. E., de Vega, R. G., Röhnelt, A., Bishop, D. P., Cole, N., et al. (2019). Low background mold-prepared gelatine standards for reproducible quantification in elemental bio-imaging. *Analyst*, *144*(23), 6881–6888. https://doi.org/10.1039/c9an01580a

Wilhelms-Dick, D. (2008). Enhanced analysis of stratified climate archives through upgrade of Laser ablation inductively coupled plasma quadrupole to time of flight mass spectrometry? (Doctoral dissertation, Universität Bremen).

## References From the Supporting Information

de Vega, R. G., Lockwood, T. E., Paton, L., Schlatt, L., & Clases, D. (2023). Non-target analysis and characterisation of nanoparticles in spirits via single particle ICP-TOF-MS. *Journal of Analytical Atomic Spectrometry*, *38*(12), 2656–2663. https://doi.org/10.1039/d3ja00253e

Lockwood, T. E., de Vega, R. G., & Clases, D. (2021). An interactive Python-based data processing platform for single particle and single cell ICP-MS. *Journal of Analytical Atomic Spectrometry*, *36*(11), 2536–2544. https://doi.org/10.1039/d1ja00297j

Lockwood, T. E., de Vega, R. G., Du, Z., Schlatt, L., Xu, X., & Clases, D. (2024). Strategies to enhance figures of merit in ICP-ToF-MS. *Journal of Analytical Atomic Spectrometry*, *39*(1), 227–234. https://doi.org/10.1039/d3ja00288h